minerals

MDPI

Article

Black Agates from Paleoproterozoic Pillow Lavas (Onega Basin, Karelian Craton, NW Russia): Mineralogy and Proposed Origin

Evgeniya N. Svetova *, Svetlana Y. Chazhengina, Alexandra V. Stepanova and Sergei A. Svetov

Institute of Geology, Karelian Research Centre of RAS, 185910 Petrozavodsk, Russia; chazhengina@mail.ru (S.Y.C.); stepanov@krc.karelia.ru (A.V.S.); ssvetov@krc.karelia.ru (S.A.S.)
* Correspondence: enkotova@rambler.ru

Abstract: The present study provides the first detailed investigation of black agates occurring in volcanic rocks of the Zaonega Formation within the Onega Basin (Karelian Craton, Fennoscandian Shield). Three characteristic texture types of black agates were identified: monocentric concentrically zoning agates, polycentric spherulitic agates, and moss agates. The silica matrix of black agates is only composed of length-fast and zebraic chalcedony, micro- and macro-crystalline quartz, and quartzine. In addition to silica minerals, calcite, chlorite, feldspar, sulphides, and carbonaceous matter were also recognised. The black colour of agates is related to the presence of disseminated carbonaceous matter (CM) with a bulk content of less than 1 wt.%. Raman spectroscopy revealed that CM from black agates might be attributed to poorly ordered CM. The metamorphic temperature for CM from moss and spherulitic agates was determined to be close to 330 °C, whereas CM from concentrically zoning agates is characterised by a lower temperature, 264 °C. The potential source of CM in moss and spherulitic agates is associated with the hydrothermal fluids enriched in CM incorporated from underlaying carbon-bearing shungite rocks. The concentrically zoning agates contained heterogeneous CM originated both from the inter-pillow matrix and/or hydrothermal fluids.

Keywords: agate; Raman spectroscopy; X-ray powder diffraction; electron scanning microscopy; Paleoproterozoic volcanics; carbonaceous matter

Citation: Svetova, E.N.; Chazhengina, S.Y.; Stepanova, A.V.; Svetov, S.A. Black Agates from Paleoproterozoic Pillow Lavas (Onega Basin, Karelian Craton, NW Russia): Mineralogy and Proposed Origin. *Minerals* **2021**, *11*, 918. https://doi.org/10.3390/min11090918

Academic Editors: Galina Palyanova and Frederick Lin Sutherland

Received: 12 July 2021
Accepted: 22 August 2021
Published: 25 August 2021

1. Introduction

Agate and chalcedony are varieties of silica that are mostly composed of minute crystals of α-quartz. Chalcedony is band-free and characterised by uniform colouration, whereas agate is defined as banded or patterned chalcedony [1]. Agates usually contain significant amounts of other silica phases (opal, cristobalite, tridymite, quartzine, moganite, macro-crystalline quartz) and paragenetic minerals (carbonates, clay minerals, zeolites, iron compounds, etc.) [2]. These impurities may be responsible for the wide diversity in colour and spectacular pattern of agates. White, bluish, and greyish colours of fine-banded agates are mainly related with microstructural features of alternating bands, including porosity and water content [3,4]. The most common agate shades are caused by Fe, Mn, Co, Cr, and some other transition elements [5]. Inclusions of iron oxides/hydroxides are responsible for red, brown, and yellow colours [3,6,7]. Different tints of green colour can be related to chlorite, epidote, or mica inclusions dispersed within the silica matrix [7–9]. Black varieties of agate are rare and have been described from a few occurrences in India, Brazil, South and Western Africa [10], and Bulgaria [3]. The black colouration of agate areas can be caused by micro-inclusions of Fe-, Mn-, and Ti-oxides [3], as well as carbonaceous material [10,11]. The origin of carbonaceous matter (CM) in agates is quite vague. For instance, it is assumed that the origin of carbon-rich inclusions in Mali agates can be related to both the hydrothermal formation of graphite from methane under elevated temperature and graphitisation of organic precursors by secondary hydrothermal or metamorphic overprint [10]. The investigation of the solid hydrocarbon (bitumen) substance in agates from Nowy Kościół (Poland) revealed its algal or algal-humic origin [11].

In the Paleoproterozoic (2100–1980 Ma) volcanic rocks within the Onega Basin (Karelian Craton, Fennoscandian Shield, NW Russia) [12], agates are widely distributed and characterised by a diversity of colours and textures. A previous study showed that the light-coloured agates from these volcanic rocks have greenish, brownish-red colour, and fine or coarse banded concentric zoning, with spotted or poor-fancy textures [13]. Black-coloured agates locally occur in this area. Timofeev (1924) was the first to discover black-coloured agates at the north-western coast of Lake Onega [14]. He called them "black agates" and supposed that the black colour is related to the disseminated carbon originating from shungite, typical for the Onega Basin [12].

The present study aims to examine the black agates from Paleoproterozoic pillow lavas within the Onega Basin. To specify the origin of black colouration and the potential source of carbonaceous matter in agates, we studied mineral and chemical compositions of agates as well as characteristics of CM. The results of mineralogical, XRD, and Raman spectroscopy investigations provided novel information on genesis of black-coloured agates from the Paleoproterozoic volcanic rocks within the Onega Basin.

2. Geological Setting

The Onega Basin with an area of more than 35,000 km^2 [15] is located in the south-eastern part of the Archean Karelian Craton in the Fennoscandian Shield (Figure 1A). The Karelian Craton is formed by granite-greenstone and tonalite-trondhjemite-granodiorite complexes of the Meso-Neoarchean [12,16–18]. The Onega Basin has developed in the Paleoproterozoic under the continental rifting regime [12].

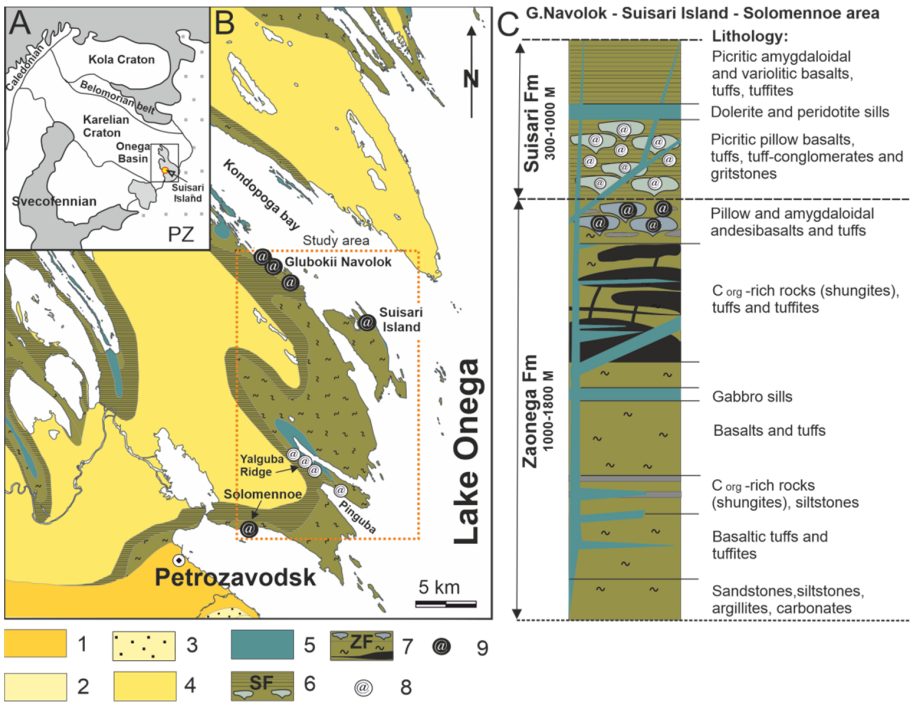

Figure 1. Location of sampling areas (**A**) and simplified geological map of the north-western part of the Onega Basin, Karelian Craton (**B**). Legend: Neoproterozoic: 1—ca. 635–542 Ma sandstones, siltstones, argillites, conglomerates. Paleoproterozoic: 2—ca. 1800–1650 Ma red quartzitic sandstones, quartzites, conglomerates; 3—ca. 1920–1800 Ma grey sandstones, siltstones, argillites, conglomerates; 4—quartzitic sandstones; 5—ca. 1975–1956 Ma gabbroids. Ludicovian Super-horizon, ca. 2100–1920 Ma: 6—picrites, picritic basalts, tuffs, tuffites, tuff-conglomerates, gritstones (Suisari Formation); 7—C_{org}-rich rocks (shungites), sandstones, siltstones, argillites, carbonates, basalts, andesibasalts, tuffs, tuffites (Zaonega Formation); 8—light-coloured agate occurrences; 9—black agate occurrences. (**C**) Simplified geological section of the studied area.

The Paleoproterozoic volcano-sedimentary successions of the Onega Basin are subdivided into six lithostratigraphic units: Sumian (2.5–2.4 Ga), Sariolian (2.4–2.3 Ga), Yatulian (2.3–2.1 Ga), Ludicovian (2.1–1.9 Ga), Kalevian (1.9–1.8 Ga), and Vepsian (1.8–1.7 Ga). The lowermost Sumian Super-horizon unconformably overlies the Archean basement. The Sariolian, Jatulian, Ludicovian, and Kalevian Super-horizons are separated from each other by unconformities and paleo-weathered surfaces [12]. The age boundaries of the formations are determined by the regional chronostratigraphic scheme [18].

Among the Paleoproterozoic volcanic-sedimentary formations of the Onega Basin, two large igneous provinces of plateau-basalts are distinguished: Yatulian dolerite-basaltic (2300–2100 Ma) [15,19] and Ludicovian picrite-basaltic (2050–1970 Ma) [12,20,21]. The agate mineralisation studied in the present work is associated with the Ludicovian volcanic rocks. The Ludicovian Super-horizon (LSH) within the Onega Basin comprises terrigenous, siliceous, carbonate rocks with high organic carbon content, as well as mafic and ultramafic volcanic complexes (Figure 1B). The LSH includes two formations (Figure 1C): the lower Zaonega Formation (ZF) and the upper Suisari Formation (SF) [22].

Zaonega Formation has a total thickness of 1100–1800 m. The base of the sequence (100–200 m) comprises alternating sandstones, siltstones, and mudstones, containing up to 3% organic carbon, and carbonates. Interbedded volcanic and sedimentary rocks prevail in the middle and upper parts of the sequence (800–900 m). Sediments are represented by carbonates and siltstones and contain 20 to 80 wt.% organic carbon [23–28], and were named "shungite rocks" after Inostrantsev [29]. Volcanic rocks include plagio-phyric massive and pillow andesibasalts with a thickness of lava flow ca. 8–35 m, tuffs, and tuffites. The ZF has been dated at 2100–1980 Ma [18,30,31].

Suisari Formation: The sequence has a total thickness of 300–1000 m and is represented by picrite-picrobasaltic massive and pillow lavas interbedded with tuff and tuffite material [12,21]. It is separated from the ZF by a horizon of tuff conglomerates, polymictic conglomerates, and gritstones, overlying the ZF with insignificant angular unconformity. The SF has been dated at 1980–1920 Ma [12,15,21].

The intrusive units of ZF and SF comprise dykes and gabbro-dolerite sills. For example, the age of quartz dolerites from the eastern Zaonezhsky Peninsula (Lebeshchina area) is 1956 ± 5 Ma [30], Konchozero gabbro-dolerite sill is 1975 ± 24 Ma [15], and Paza-Kochkoma gabbro-dolerite sill is 1961.6 ± 5.1 Ma [31].

Pillow lavas formed in shallow underwater environments dominate among the ZF and SF of LSH volcanic rocks. The pillows that range in size from 0.5 to 4 m are differentiated and have thin (<1 cm) chill zones, a fine-grained marginal part, and a medium-grained core. The composition of pillow lavas ranges from basaltic andesite in ZF to picrobasalts in SF. Variolitic structure in the pillows was recognised in the lower part of the SF and is absent in ZF [32–34]. The inter-pillow matrix is represented by lava breccia, tuff, tuffites, or sandstones, sometimes with an admixture of CM. The occurrence of CM is typical for pillow lavas from the upper part of ZF and rarely recorded in the pillow lavas from the lower part of SF. The central parts of the pillows are gas-saturated, which is evidenced by numerous amygdales (0.3–1 cm) and large (0.3–0.6 m) gas vesicles filled by light-coloured and black agates [9].

Available geochronological data indicate that in most parts of the Onega basin, the LSH volcanic, intrusive, and sedimentary rocks, including shungites, were deformed and metamorphosed at ca. 1780–1750 Ma [35,36]. The ZF and SF successions in the studied area experienced prehnite-pumpellyite facies metamorphism under T: 290–320 °C, P: 1–3 kbar [36].

The earliest interval of hydrothermal alteration of the LSH in the ZF is associated with the injection of gabbro-dolerite sills of age 1970–1950 Ma. The sills are triggered hydrothermal fluid flow, redistribution of carbonaceous material, and epigenetic sulphide mineralisation [37]. The Rb-Sr isotope study of altered rocks in the Onega Basin [38] revealed several subsequent peaks of hydrothermal activity at 1780–1700, 1600, and 1500 Ma. The

1780–1700 Ma events were assumed to be related to doleritic sills of an age 1770 ± 12 Ma (U-Pb, zircon [39]) or late Svecofennian orogenic events [38].

3. Agate Occurrence

Agates from pillow lavas along with the inter-pillow matrix were collected from the coastal outcrops of the Petrozavodsk and Kondopoga bay of Lake Onega at the following occurrences: Suisari Island, Glubokii Navolok, and Solomennoe (Figure 1B). Three representative black agate samples with the size varying from 3 to 10 cm with various textures were selected for investigation. Additionally, three samples of inter-pillow matrix from basaltic pillow lavas of Solomennoe occurrences were sampled for comparison.

(1) Suisari Island. In the north-eastern part of the Suisari Island (Keltnavolok cape) (Figure 1B), the ZF plagio-phyric pillow lava flows with a thickness of 25 m are exposed. The pillows are slightly deformed and have chill zones up to 1 cm, fine-grained marginal zones, and a coarse-grained core, and their diameter ranges from 0.5 to 4–5 m. The central and upper parts of the pillows contain gas cavities filled by chalcedony and calcite, sometimes with carbonaceous material. The agates have a black colour. Along with black agates, light-coloured quartz-carbonate-chlorite varieties of agates are widely distributed in the outcrops [9,13]. The inter-pillow matrix is composed of chloritized lava breccia and tuff material. There are numerous cavities in the inter-pillow matrix filled by chalcedony, calcite, and carbonaceous material that form agates with a size up to 70 cm.

(2) Glubokii Navolok cape. The coastal outcrops of Kondopoga bay from Suisari village to Glubokii Navolok (Figure 1B) are formed by the volcano-sedimentary succession that belongs to the lower part of the SF and upper part of the ZF. In this area, the LSH section comprises massive and pillow picrobasalts (SF), plagioclase-pyroxene, and pyroxene-phyric basalts interbedded with lava breccias, agglomerate, and pyroclastic tuffs (ZF). The thickness of lava flows ranges from 5 to 16 m. The agate mineralisation is mainly associated with pillow lava flows and pyroclastic tuffs matrix (ZF, Figure 2A–C). The rounded, elongated pillow-shave chill zones range up to 1 cm and have well-developed sagging tails. The diameter of pillows varies from 0.5 to 3 m. Agates fill cavities in the inter-pillow space, fissures, and gas vesicles in pillow lavas, and are also observed in pyroclastic tuffs. The size of agates ranges from 3 to 25 cm. They are composed of quartz-carbonate material with organic carbon impurities.

(3) Solomennoe. The coastal outcrops near Solomennoe village (Figure 1B) are represented by massive and pillow lavas of plagioclase-phyric basalts (upper parts of ZF). Some pillows have flow banding—pahoehoe. Massive and pillow lavas are often interbedded with lenses of basaltic carbon-rich tuffs and tuffites [15] (Figure 2D,E) that are 20–40 cm in thickness and up to 12 m along the strike. The interbeds are black in colour and often bordered by pillows by thin films. A series of thin picrobasaltic dykes cut the lava flows and overlay sedimentary succession. The hydrothermal alteration is widespread in the pillow lavas at the boundary with dykes, and large carbonate nests (up to 1 m in size) are noted. The agates in this area are rare and were identified exclusively in the cores of large pillows and are represented by light-coloured varieties.

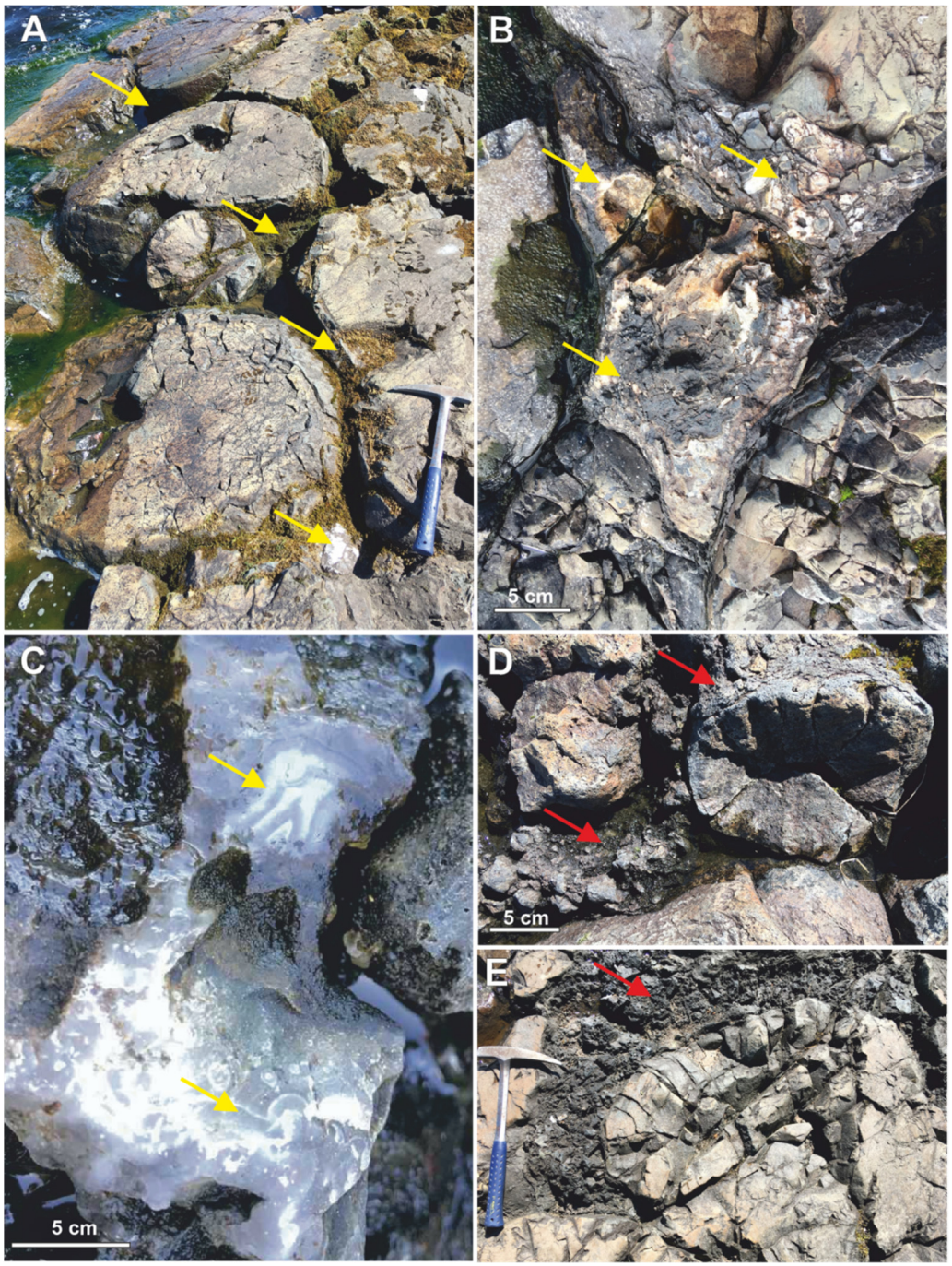

Figure 2. Field outcrop photographs illustrating black agates' location in the Paleoproterozoic volcanics within Onega Basin LSH (ZF). (**A**) Agates in gas vesicles and inter-pillow lava space (Glubokii Navolok), (**B**) agates in the inter-pillow lava space (Glubokii Navolok), (**C**) banded agates in the inter-pillow lava space (covered by water) (Glubokii Navolok), and (**D**,**E**) interbeds of carbon-rich rock ("shungite") in the inter-pillow lava space (Solomennoe). Yellow arrows point to the black agates, and red arrows to carbon-rich rock.

4. Methods

The black agates and inter-pillow matrix were studied using optical and scanning electron microscopy (SEM), electron microprobe analysis, X-ray powder diffraction, X-ray fluorescence spectrometry, thermal analysis, and Raman spectroscopy. Analytical investigations of the agates were carried out at the Institute of Geology, Karelian Research Centre, RAS (IG KRC RAS, Petrozavodsk, Russia).

Standard petrographic analyses were carried out using a Polam-211 optical microscope.

Scanning electron microscopy (SEM) and energy-dispersive X-ray spectrometry (EDS) investigations were applied to study the micromorphological features and chemical composition of individual agate zones. The experiments were performed using a VEGA II LSH (Tescan, Brno, Czech Republic) scanning electron microscope with an INCA Energy 350 energy-dispersive detector (Oxford Instruments, Oxford, UK) at the following parameters: W cathode, 20 kV accelerating voltage, 20 mA beam current, 2 μm beam diameter, and counting time of 90 s. Agate chips were coated by a carbon layer. Polished thin sections of agates were coated with a thin beryllium layer for quantity analysis of carbon content. The following standards were used: calcite, albite, MgO, Al_2O_3, SiO_2, FeS_2, wollastonite, Fe, Zn, InAs, and C (graphite). SEM-EDS quantitative data and determination of the analysis accuracy were acquired and processed using the Microanalysis Suite Issue 12, INCA Suite version 4.01. Standard deviation (SD) for Si: 0.5–0.7%, and for C: 1.0–1.1%. The average composition of the black and white agate zones was determined by the EDS microanalysis.

Powder XRD analysis was carried out using a Thermo Scientific ARL X'TRA (Thermo Fisher Scientific, Ecublens, Switzerland) diffractometer (CuKα-radiation (λ = 0.1790210 nm), voltage 40 kV, current 30 mA). All samples were scanned for review in the 2–80° 2θ range at a scanning step of 0.6° 2θ/min. Diffractograms in the 66–69° 2θ range were recorded at a scanning step of 0.2° 2θ/min for more precise measurements of parameters of diffraction reflections. X-ray phase and structural analyses were carried out using the program pack Win XRD, ICCD (DDWiew2008). Agate samples were hand-ground to obtain grain sizes < 50 μm. The detection limit for XRD phase identification was 3%.

The chemical composition of the agate samples was determined by X-ray fluorescence (XRF) using an ARL ADVANT'X-2331 (Thermo Fisher Scientific, Ecublens, Switzerland) wavelength-dispersive spectrometer with a rhodium tube, working voltage of 60 kV, working current of 50 mA, and resolution of 0.01°. Preliminarily, 2 g of each powdered sample were heated in ceramic crucibles at 1000 °C in a muffle furnace for 30 minutes. The loss of ignition was determined by a change in the mass of the sample after heating. For XRF measurements, 1 g of heated sample was mixed with Li-tetraborate flux and heated in an Au-Pt crucible to 1100 °C to form a fused bead.

Thermal properties of the agates were examined on a NETZSCH STA 449 F1 Jupiter (Selb, Germany) equipment. The powdered samples were placed into a platinum-rhodium crucible in the amount of 10 mg. The analysis was performed over the temperature range of 20–1200 °C in the air atmosphere at a rate of 10 °C/min.

Raman spectroscopy was used to investigate the structural characteristics of the carbonaceous matter recorded in agates. Raman spectroscopy analysis was carried out using a dispersive Nicolet Almega XR Raman spectrometer (Thermo Fisher Scientific, Waltham, MA, USA) with a green laser (532 nm, Nd-YAG) (Thermo Fisher Scientific, Waltham, MA, USA). The spectra were collected at 2 cm^{-1} spectral resolution. The spectrometer was calibrated before each analytical session by 'zero-point' centring and by analysing a Si-standard with a characteristic Si Raman band at 520.4 cm^{-1}. A confocal microscope with a 50× objective was used to focus an excitation laser beam on the sample and to collect a Raman signal from a 2 μm diameter area. Raman spectra were acquired in the 85–4000 cm^{-1} spectral region, with the exposition time between 30 and 100 s for each scan, depending on the signal intensity, and laser power of 2–10 mW to prevent any sample degradation. A total of 75 Raman spectra were acquired from polished cross-sections and thin sections.

A Raman spectrum of CM is composed of two intensive G and D1 bands in the first-order region (1100–1800 cm^{-1}). The graphite band G (~1580 cm^{-1}) corresponds to the in-plane vibration of aromatic carbons in the graphitic structure [40]. The bands D1 (~1350 cm^{-1}) and D2 (~1620 cm^{-1}) appear in disordered CM, and they are assigned to defects in the graphitic structure [40–42]. In poorly ordered CM, at least two additional peaks, D3 (~1500 cm^{-1}) and D4 (~1260 cm^{-1}), can be decomposed in the first-order region of the CM Raman spectrum. Broad D3 band results from out-of-plane defects, related to tetrahedrally coordinated carbons, dangling bonds, and heteroatoms, occur in natural CM [40,41]. In poorly ordered CM, the D4 band appears like a shoulder of the D1 band (~1190–1250 cm^{-1}). It has been tentatively attributed to sp^2–sp^3 bonds or C–C and C=C stretching vibration of polyene-like structures [43,44].

The most intensive bands in the second-order region of CM Raman spectra are located at ~2700 and ~2900 cm^{-1}. The former is attributed to overtone scattering of the D1 band and is absent in poorly ordered CM, while in pure crystalline graphite, it occurs as a doublet of two partially overlapping peaks [41]. The later is attributed to the combination modes (G + D) and appears only in poorly ordered CM or is due to the presence of C–H; bonds [40–42].

For peak decomposition, we used the band protocol described by Kouketsu et al. [45]. Raman spectral data, such as peak position, band area (i.e., integrated area), and band width (i.e., full-width at half maximum (FWHM)), were determined using OMNIC for Dispersive Raman software v.8.2. (v.8.2., Thermo Fisher Scientific, Waltham, MA, USA) with a Gaussian/Lorentzian function. Mean values, estimated for each sample from several spot analyses, and standard deviation, which may characterize the heterogeneity of the carbonaceous matter of a sample, were calculated for each parameter of the Raman spectrum.

5. Results

The agates from ZF with a black and white pattern mostly occur in the inter-pillow lava space as veinlets and prominent nodules. They were also rarely observed within the tuffs matrix. The agates exhibit alternating white and black non-transparent zones, significantly varying in amount and size (Figure 3A–G). The black colour of local agate areas (as shown below) is related to the presence of disseminated CM in the silica matrix. In some cases, agates contain cavities encrusted by quartz druses or sinter chalcedony (Figure 3A). Three texture types of black agates from ZF were identified, including monocentric concentrically zoning agates, polycentric spherulitic agates, and moss agates.

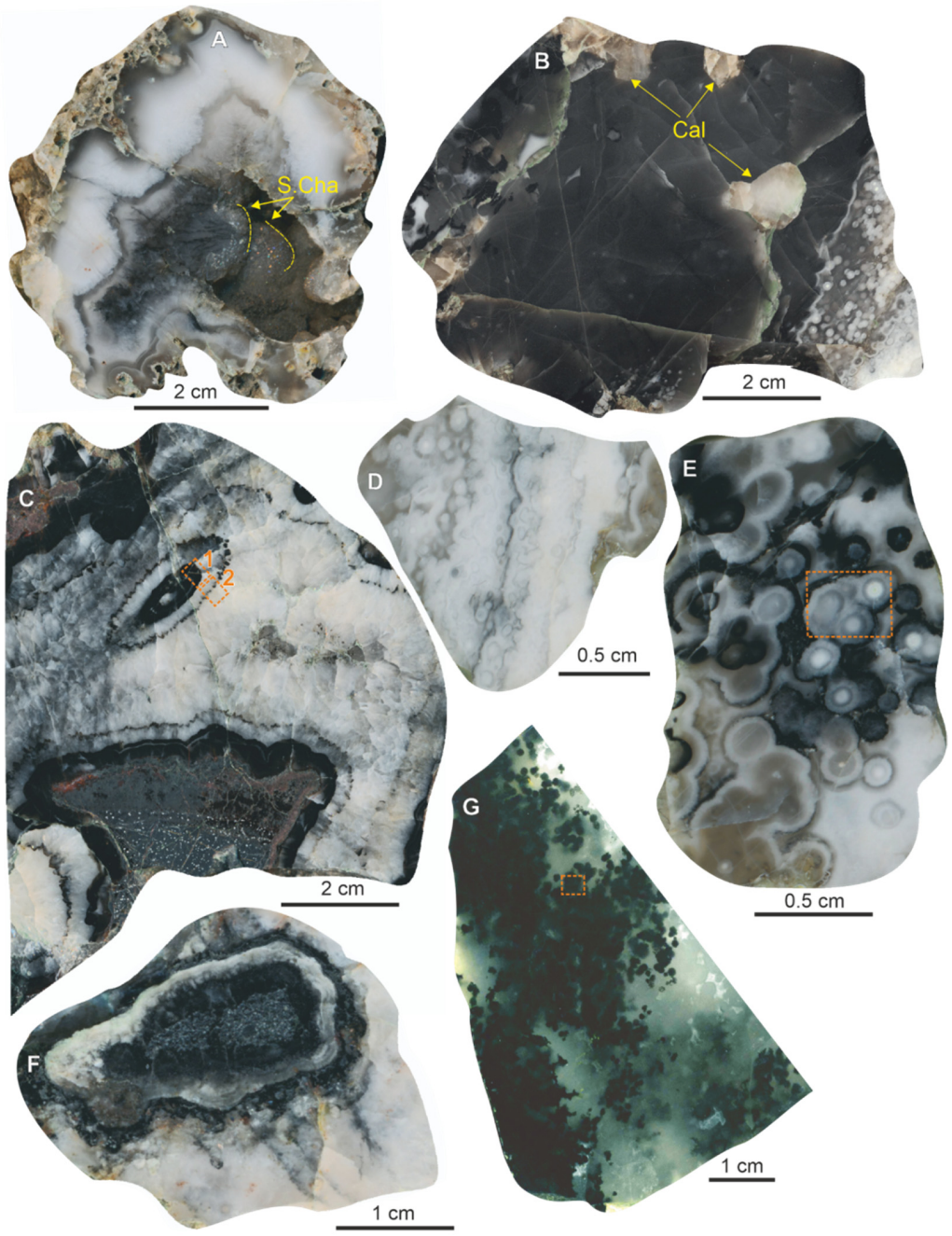

Figure 3. Photographs of Onega black agates in the Paleoproterozoic volcanics within the Onega Basin LSH (ZF). (**A**) Concentrically zoned agate with central cavity covered by sinter chalcedony (Glubokii Navolok), (**B**) uniform opaque agate with quartzine spherulites zone and large calcite inclusions (Suisari Island), (**C**) concentrically zoning agate with black ellipsoid (Suisari Island), (**D**) enlarged fragments of spherulitic zone from (**B**), (**E**) black and white spherulite agate (Glubokii Navolok), (**F**) concentrically zoned agate (Glubokii Navolok), (**G**) moss agate composed by colourless chalcedony with black-rounded segregations of carbonaceous matter (Suisari Island). S. Cha—sinter chalcedony, Cal—calcite. The areas of optical microscopy analysis are marked with orange squares, explanations in Figure 4.

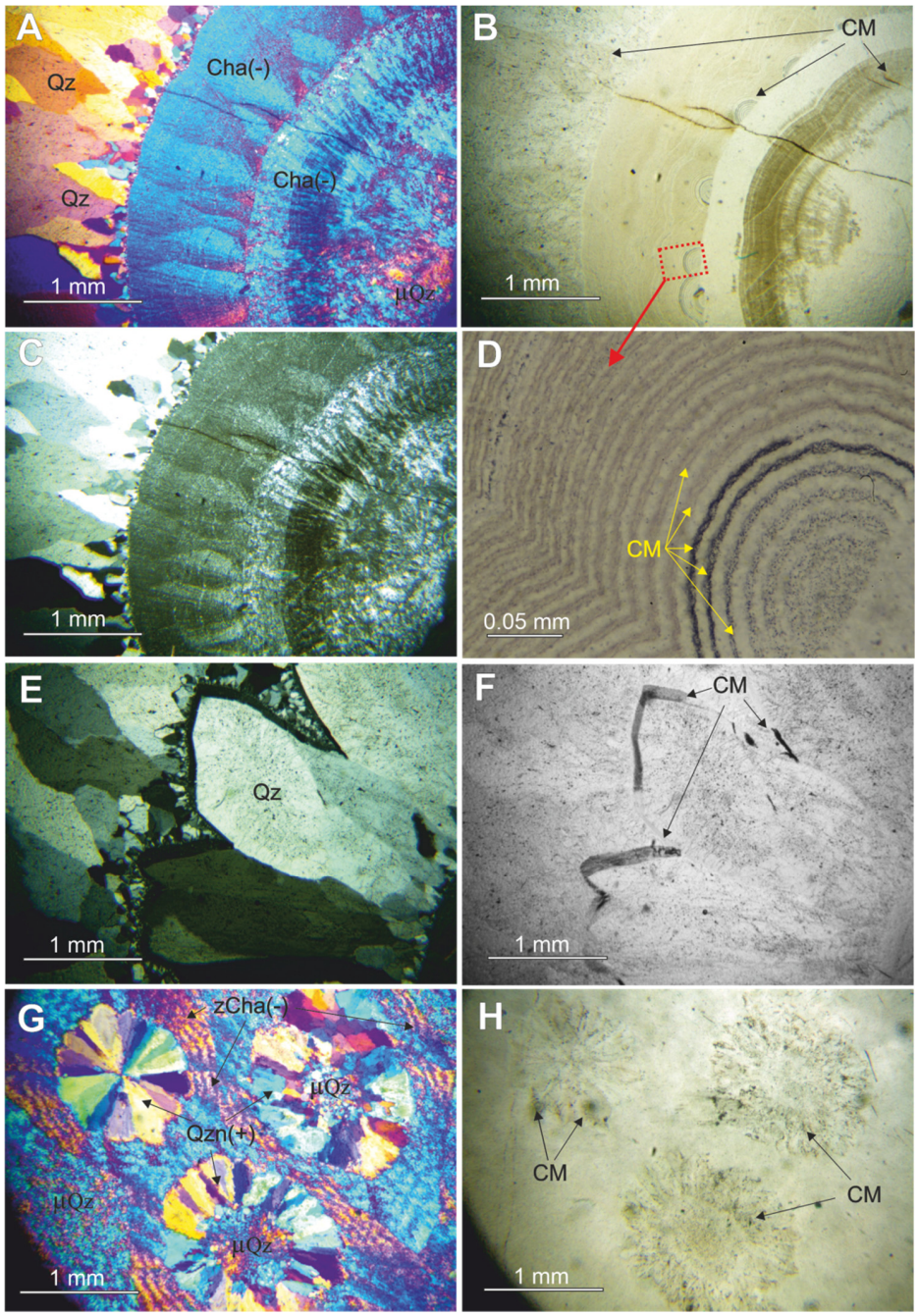

Figure 4. Microphotographs of black Onega agates with disseminated carbonaceous matter (CM): (**A**–**C**) fragment of the black concentric ellipsoid (from selected area 1, Figure 3C) with alternating zones of length-fast chalcedony, micro- and macro-crystalline quartz in concentrically zoning agate. (**D**) Enlarged fragment (from selected area of (**B**)) with fine concentric bands of chalcedony, between which CM is disseminated. (**E**,**F**) Fragment of the black concentric ellipsoid (from selected area 2, Figure 3C) with black jagged band containing carbonaceous pigment developed at the edges of euhedral prismatic quartz crystals (Figure 3C, area 2). (**G**,**H**) Spherolites of radial fibrous quartzine in microcrystalline quartz matrix with zebraic chalcedony zones (Figure 3E). (**A**,**G**) Polarised light, crossed nicols, compensator plate. (**C**,**E**) Polarised light, crossed nicols. (**B**,**D**,**F**,**H**) Plane polarised light. (**B**,**D**,**F**,**H**) Photos show that the macroscopic black colour is caused by an accumulation of CM in the local agate zones. Abbreviations: Cha(−): length-fast chalcedony; zCha(−): zebraic chalcedony; Qzn(+): length-slow chalcedony (quartzine); Qz: macrocrystalline quartz; µQtz: microcrystalline quartz.

5.1. Macro- and Micro-Scopic Characteristics

Concentrically zoning agates (CZ), recognised as nodules, exhibit alternating black and white bands (Figure 3C,F). Black bands are usually localised parallel to the outer shell of an agate nodule close to the contact with the host rock. The thickness of black bands ranges from 0.3 mm to 1 cm. Additionally, black ellipsoids with a size of up to 2 cm were recognised in the inner white part of CZ agates. The petrographic study revealed that the silica matrix of CZ agates is comprised of alternating layers of length-fast chalcedony (with the c-axis situated perpendicular to the fibres), and micro- and macro-crystalline quartz (Figure 4A–C). The thick black bands in the outer part of agates and black ellipsoid inside nodules (Figure 3C) under low magnifications appear to be uniform and completely formed by CM, whereas under high magnification, it shows that they consist of numerous fine concentric bands of microcrystalline quartz and chalcedony, between which carbonaceous matter is disseminated (Figure 4B,D). CM in CZ agates are mostly concentrated in zones of fine-grained quartz and chalcedony. The black jagged bands containing carbonaceous pigment with a thickness up to 0.3 mm occur both in the margins and central parts of the nodules around the ellipsoid (Figure 3C). The optical microscopic study revealed that these bands repeat the morphology of the boundary of the macrocrystalline quartz zone and mark the termination of individual zone crystallisation in banded agate (Figure 4E,F).

Spherulitic agates (SP) occur in the inter-pillow space as nodules. They are represented by black, grey, and white spheroliths with a size of up to 3 mm embedded in a silica matrix (Figure 3D,E), and some of them are coalescent. SP agates contain un-zoned and concentrically zoning spherulites (Figures 3B,D,E and 4G,H). Un-zoned spherulites are composed only of radial fibrous quartzine (length-slow chalcedony with the c-axis situated parallel to the fibres), whereas zoned spherulites comprise a microcrystalline quartz core rounded by a concentric layer of fibrous quartzine (Figure 4G). CM is concentrated within the quartzine fibres and, to a lesser extent, between microcrystalline quartz grains (Figure 4H). Silica matrix-contained spheroliths are represented by microcrystalline quartz and zebraic chalcedony (length-fast with a helical twisting of fibres along the c-axis) (Figure 4G).

Moss agates (MS) are the rarest variety of black agates recognised in ZF. They occur as veinlets in the inter-pillow space. MS agates are composed of transparent colourless chalcedony with numerous black rounded segregations with a size of about 1 mm (Figure 3G). The microscopical study under high magnification in plane polarised light revealed that the black segregations do not have clear contours (Figure 5A,B). The microstructure of the MS agates is presented by microcrystalline quartz (Figure 5C). CM in black segregations is accumulated predominantly between quartz grains (Figure 5D). The micrographs in transmitted light (crossed nicols) of the black segregation area (Figure 5C) of the MS agate show that concentrating of CM is associated with the zones containing finer chalcedony grains.

Inter-pillow matrix is represented by agglomerate tuffs and tuffites of basaltic composition interbedded by the thin layers composed of quartz, calcite, and CM. The inter-pillow matrix has strongly heterogeneous composition within the lava flows. According to the microscopic observation and XRD and Raman analyses, it comprises augite, plagioclase, chlorite, prehnite, calcite, quartz, and CM.

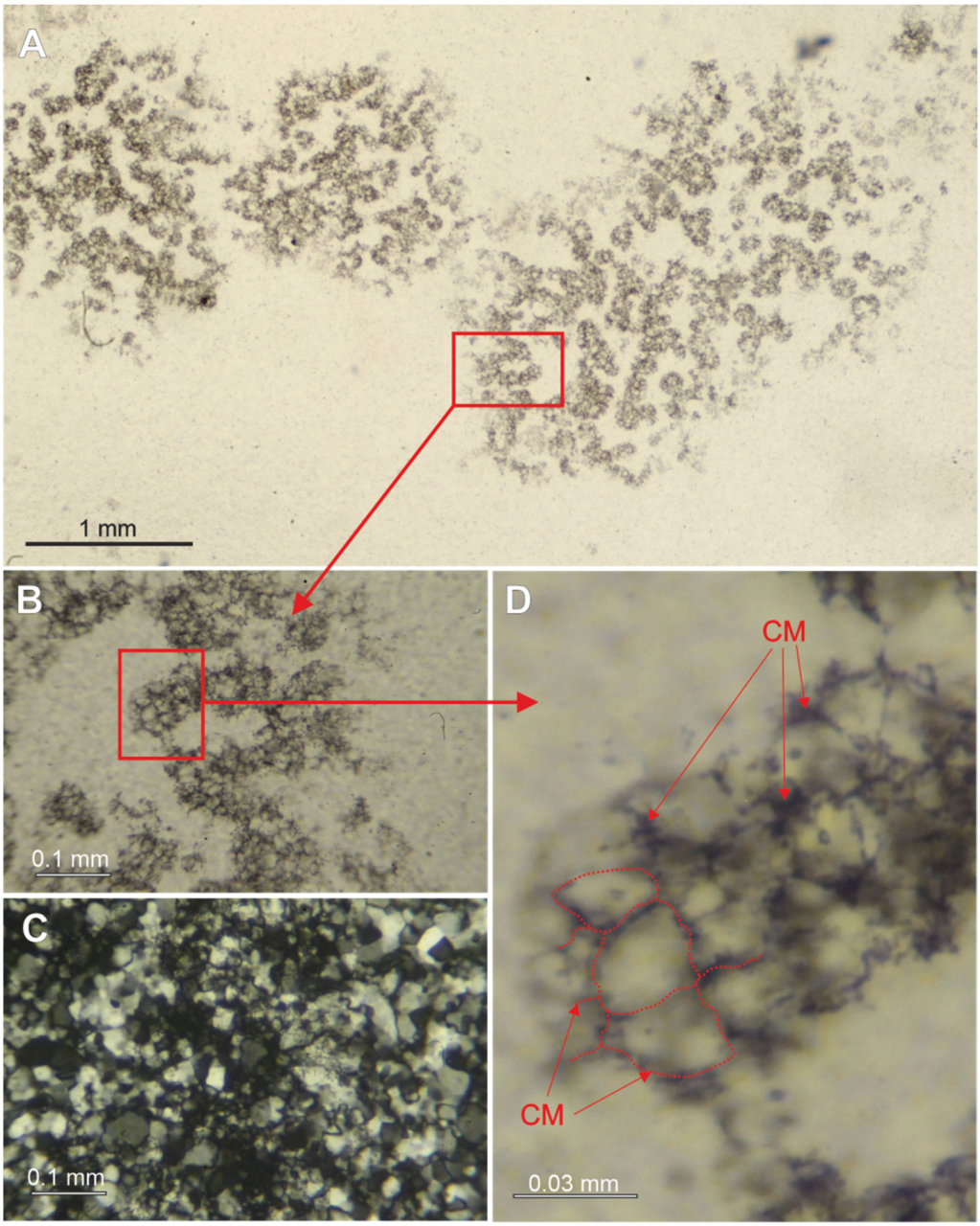

Figure 5. Microphotographs of moss agates (Figure 3G): accumulations of disseminated carbonaceous matter (CM) within the chalcedony matrix in transmitted light (**A**), enlarged fragment from the dark rounded segregation (as indicated in (**A**)) in transmitted light (**B**), and the same fragment between crossed nicols (**C**). (**D**) Enlarged fragment of selected area from (**B**), red dotted lines and arrows shows CM distribution between chalcedony grains.

5.2. Mineral Composition

The phase composition of black agates was studied by the X-ray powder diffraction method. White and black parts of CZ agate, as well as bulk samples of MS and SP agates, were examined separately. Only reflections conforming to α-quartz have been identified on the diffraction patterns (Supplementary Figure S1). No other silica phases (opal, cristobalite, tridymite, and moganite) were found. Raman spectroscopy analysis is in accordance with the X-ray diffraction data showing that agates of all types are composed of α-quartz identified by the characteristic bands at 465, 358, 210, and 130 cm^{-1} (Supplementary Figure S2).

All obtained diffraction patterns are characterised by well-developed reflections, (212), (203), (301), corresponding to macrocrystalline quartz. The quartz crystallinity index (CI) of agate is calculated from the peak resolution in the (212) reflection at 2θ ≈ 67.74°, as CI = 10Fa/b, following the method in [46] (Figure 6). A colourless quartz crystal from hydrothermal metamorphogenic veins of the Subpolar Urals (Russia) [47] served as a reference standard, with CI = 10. Quartz from the white agate area (CZw) displays higher CI values (10.3) as compared to quartz from the black agate area (CZb) (CI = 9.9), SP (CI = 9.5), and MS (CI = 9.9). No graphite phase or traces of CM were observed on diffractograms (Supplementary Figure S1).

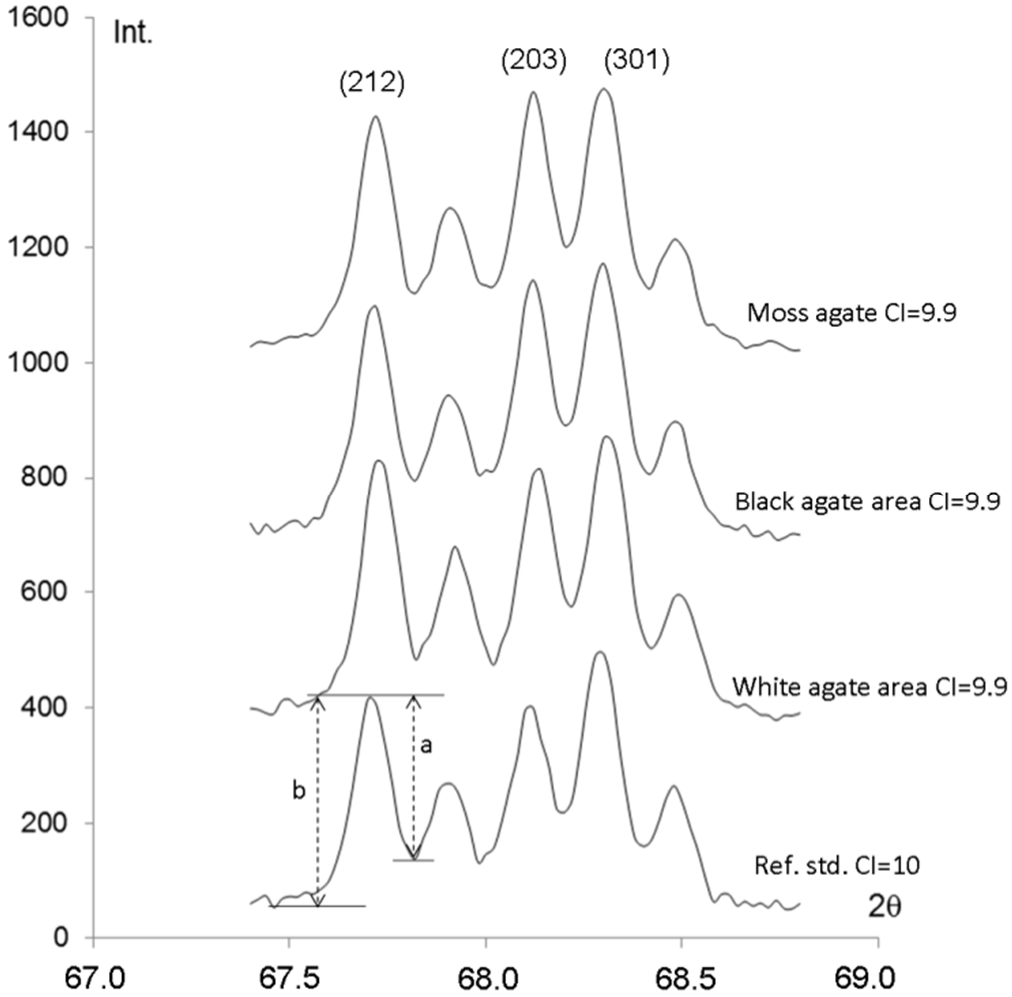

Figure 6. Fragments of X-ray diffractograms of the spherulitic agate, moss agate, black and white agate of concentrically zoning agate, and quartz crystal (Ref. std., Subpolar Urals), with the 2θ 68° quintuplet peak. a and b parameters are measured for Crystallinity Index (CI) calculation.

Scanning electron microscopical and microprobe investigations of agates revealed various mineral micro-inclusions, both in the black and white areas of all agate types. The most frequent inclusions were established as calcite in the form of macro- and micro-inclusions (Figure 7A,B). Micro-inclusions of K-feldspar and chlorite are also characteristic of all types of agates (Figure 7C). Pyrite, sphalerite, and arsenopyrite were recognised in black and white agate areas (Figure 7D–F). Iron oxides/hydroxides inclusions, typical of light-coloured varieties of agates of LSH [9,13], are rare in black agates.

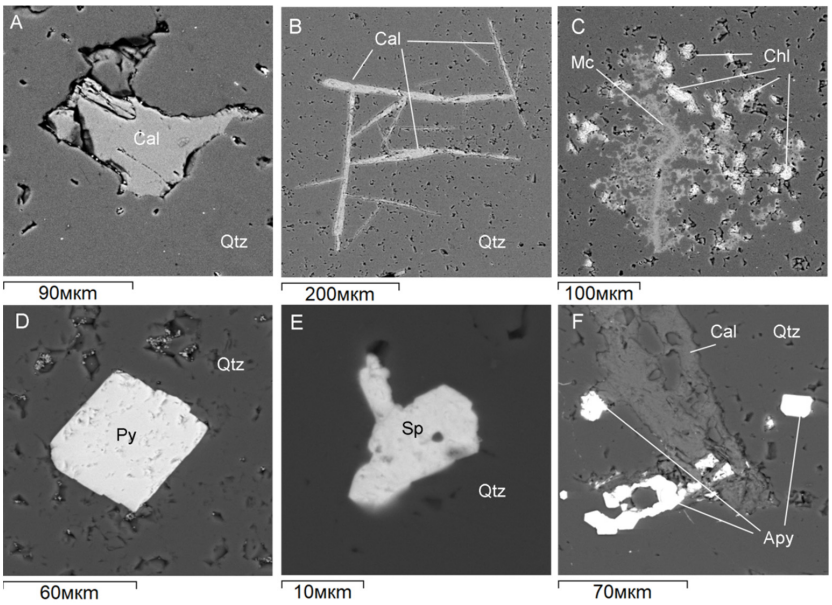

Figure 7. BSE images of micro-inclusions in black Onega agates: (**A**) calcite inclusion in the white area of the concentrically zoning agate, (**B**) calcite (Cal) inclusions in the black marginal area of quartzine spherolithe in spherulitic agate, (**C**) microcline (MC) and chlorite (Chl) in the white area of spherulitic agates, (**D**) prysmatic pyrite (Py) crystals in the colourless area of moss agate, (**E**) sphalerite (Sp) crystal in moss agate, and (**F**) quartz (Qtz) fissure filled by calcite, and accumulations of arsenopyrite (Apy) crystals in spherulitic agate.

Thermal analysis was applied to determine carbon content in white and black areas of CZ agate, as well as in bulk samples of MS and SP agates and the inter-pillow matrix. As a result of high-resolution thermogravimetric analysis and differential thermal analysis, several curves (TG, DTG, DSC, and dDSC) were obtained for each sample (Supplementary Figure S3). On DSC curves of all agate samples, a strong endothermic effect with a maximum at 569 °C was observed. This "quartz peak" is attributed to quartz $\alpha-\beta$ polymorph transition. On DSC curves of CZ, MS, and SP agates, and inter-pillow matrix samples in the temperature range of 500–670 °C, thermal effect attributed to carbon matter combustion [48,49] was detected. The loss in mass resulting from carbon matter combustion is 0.36% for MS agate, 0.18% for SP agate, and 0.69% for black and 0.05% for white areas of CZ agate (Table 1). The maximum carbon content of 1.87 wt.% was determined for the inter-pillow matrix.

Table 1. TG and DSC results for the black agates from the ZF of the Onega Basin.

Sample	Reaction	Temperature Range, °C	Mass Loss, %
CZw	Quartz transition	568.3	-
	Carbonaceous matter combustion	500–611	0.05
CZb	Quartz transition	568.9	-
	Carbonaceous matter combustion	474–669	0.69
MS	Quartz transition	569.2	-
	Carbonaceous matter combustion	534–652	0.36
SP	Quartz transition	568.9	-
	Carbonaceous matter combustion	580–672	0.18
IPM	Sulphide decomposition	460	0.63
	Carbonaceous matter combustion	527	1.87
	Calcite decomposition	746	11.77

Note: The measurements were performed using high-resolution thermal analysis. Samples: white (CZw) and black (CZb) agate areas of concentrically zoning agate, MS: moss agate, SP: spherulitic agate, IPM: inter-pillow matrix with carbonaceous material.

5.3. Chemical Characterisation

X-ray fluorescence spectrometry was used to provide information about the chemical composition of the black and white agate areas of CZ agate, as well as bulk samples of MS and SP agates (Supplementary Table S1). The studied samples are mainly composed of SiO_2 (97.8–98.7 wt.%) and have close contents of other oxides: Al_2O_3 (0.2–0.5%), FeO_{tot} (0–0.7%), CaO (0.5–0.7 wt.%), K_2O (0–0.1 wt.%), MgO (0.2–1.2), and TiO_2 (0.03–0.04 wt.%). The difference in value of losses on ignition (LOI) is established. The dark samples (black agate area of CZ agate and MS agate) exhibited a higher LOI (0.41 and 0.75 wt.%) than the white areas of CZ agate (0.27 wt.%). The lowest value of LOI (0.06%) was determined in SP agate.

The concentrations of the C, Si, and O in the local parts of the black and white (or colourless) areas in CZ, MS, and SP agates revealed differences in the carbon content of the black and white agate areas for all samples (Supplementary Table S2). The carbon content in the MS agate ranges from 10 to 19 wt.% in black to 5–9 wt.% in colourless areas, respectively. The CZ and SP samples are characterised by similar values of carbon content in black (6–12 wt.%, 7–13 wt.%) and white (2–6 wt.%, 4–7 wt.%) agate areas.

5.4. Characteristics of Carbonaceous Matter

The Raman spectra for carbonaceous material from all agate samples and the inter-pillow matrix are consistent with poorly ordered CM [40,41,50–52], because the first-order region of the Raman spectra shows two well-resolved bands: D1 at about 1350 cm^{-1} and G band at about 1600 cm^{-1} (Figure 8). It is noteworthy that the Raman spectra of CM in studied agates always contained the bands of admixture phases, commonly quartz and calcite. The results of spectrum decomposition for CM from agate samples showed the occurrence of two additional disorder-related bands, D3 (~1500 cm^{-1}) and D4 (~1260 cm^{-1}) (Supplementary Table S3). The low-intensity D2 band, which appeared in relatively ordered carbonaceous material [40,41,50–52], was established only in a few Raman spectra of CM from moss agates. In the second-order region, CM from all agate samples is mainly characterised by weak bands located at 2900 and 3200 cm^{-1}.

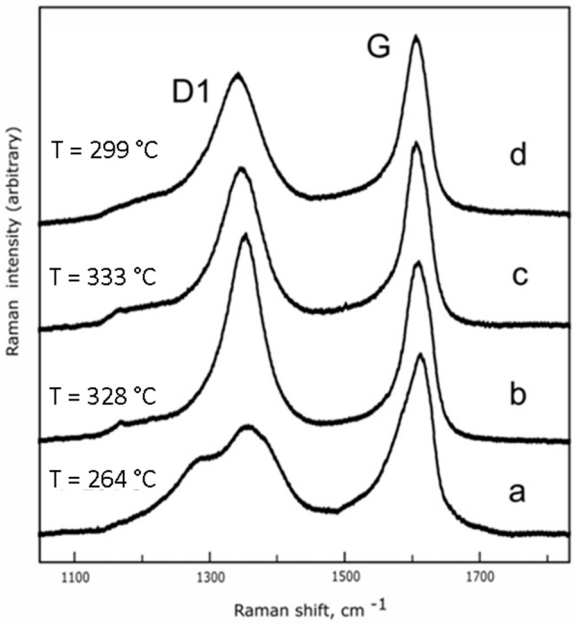

Figure 8. Representative Raman spectra of carbonaceous matter from concentrically zoning (**a**), spherulitic (**b**), and moss (**c**) agates, and inter-pillow matrix (**d**). Calculated metamorphic temperatures refer to the average value (calculated on the basis of 26 measurements for (**a**), 11 for (**b**), 10 for (**c**), and 28 for (**d**)).

However, in spite of the general similarity of CM Raman spectra, there are significant differences in Raman spectroscopic characteristics of CM from various agate types.

CM from CZ agates is characterised by parameter R1 (intensity-based ratio I_D/I_G) = 0.78 ± 0.06 and the high value of the FWHM-D1 = 99 ± 7 cm^{-1}. CMs from CZ agates have the significant scattering of both parameters R1 and FWMH-D1, which corresponds to the high degree of CM heterogeneity. Additionally, the decomposition of Raman spectra of CM from CZ agates shows that the D2 band is absent and the D3 and D4 bands have relatively high intensities; moreover, the latter might appear as a well-pronounced shoulder of the D1 band (Figure 8).

The Raman spectrum of CM from moss (MS) agate is characterised by a higher value of R1 = 0.93 ± 0.05 than the CM from CZ agates. However, the CM from moss agate has a significantly lower FWHM-D1 = 67 ± 0.5, varying in the narrow limits from 66 to 69 cm^{-1}. Unlike the CM from CZ agates, the scattering of the FWHM-D1 parameter for CM from moss agate is low, suggesting its low heterogeneity. The intensities of the D3 and D4 bands in the Raman spectra of CM from moss agates are lower than that of CZ agates (Supplementary Table S3). The D2 band has low intensity or is absent.

CMs from spherulitic (SP) agates are characterised by the higher value of R1 = 1.13 ± 0.5 compared to CZ and MS agates, and a value of FWMH-D1 = 70 ± 4 cm^{-1}, close to MS agates. The degree of scattering of R1 and FWMH-D1 parameters is intermediate between CM from CZ and MS agates. Additionally, the intensities of D3 and D4 bands in the Raman spectra of CM from SP agates have intermediate values between high in CZ agates and low in MS agates. The D2 band is absent similar to the CM from CZ agates.

CM from the inter-pillow matrix is characterised by R1 = 0.90 ± 0.05 and a high value of the FWHM-D1 = 83 ± 4 cm^{-1}. Similar to the CM from CZ agates, CM from the inter-pillow matrix have significant scattering of FWMH-D1, which might correspond to the high degree of CM heterogeneity. Additionally, similar to the CZ agates, the D2 band is absent and the D3 and D4 bands have relatively high intensities; moreover, the latter might appear as a well-pronounced shoulder of the D1 band (Figure 8) (Supplementary Table S3).

6. Discussion

6.1. Agate Varieties in the Onega Basin

Agates are widely distributed in the LSH within the Onega Basin and are mostly associated with the pillow lavas, and to a lesser extent with the massive lavas and pyroclastic tuffs. The previous study of agates [9] revealed that (Figure 1B) only light-coloured agates without carbonaceous material occurred in the lower part of SF (Yalguba Ridge, Pinguba, and Tulguba occurrences), whereas the black agates were not recorded. The light-coloured agates have greenish and brownish-red colours associated with the accessory minerals such as chlorite, phengite, epidote, and iron oxide/hydroxide. The light-coloured agate varieties occur in the inter-pillow lava space as lenses, veinlets, prominent nodules, as well as are gas vesicles' infill. They have fine- or coarse-banded concentric zoning and spotted or poor-fancy textures. Additionally, only a few light-coloured agates have been recorded in the upper part of ZF [9]. Their textural and mineralogical characteristics are similar to that of light-coloured agates from SF (Table 2).

Table 2. Summary of morphology, textures, and mineral composition of black- and light-coloured agates from Paleoproterozoic volcanics, Onega Basin.

Agate Type	Occurrences (Formations)	Colour	Morphology	Silica Phases	Mineral Association	Raman Characteristics of Carbonaceous Matter (Average Value, Standard Deviation, Minimum and Maximum Values)		
						R1	FWMH-D1, cm^{-1}	T, °C TT
Black agates								
Concentrically zoning (CZ)	Suisari Island (ZF)	Black and white	nodule	micro- and macrocrystalline quartz, length-fast chalcedony	calcite, carbonaceous matter, chlorite, hematite, sphalerite	0.78 ± 0.06 (0.62–0.94)	99 ± 7 (76–112)	264 ± 16 (230–314)
Spherulitic (SP)	Glubokii Navolok (ZF)	Black and white	nodule	microcrystalline quartz, zebraic chalcedony, quartzine	calcite, carbonaceous matter, chlorite, arsenopyrite, sphalerite	1.13 ± 0.05 (1.00–1.30)	70 ± 4 (62–81)	328 ± 8 (345–304)
Moss agate (MS)	Suisari (ZF)	Colourless with black segregations	veinlet	microcrystalline quartz	calcite, carbonaceous matter, pyrite	0.93 ± 0.05 (0.89–1.04)	67 ± 0.5 (66–69)	333 ± 1 (329–336)
Typical varieties of light-coloured agates [9]								
Concentrically zoning	Pinguba (SF)	Brownish red	amygdule	micro- and macrocrystalline quartz, length-fast chalcedony	chlorite, epidote, calcite, hematite, goethite, pyrite	-	-	
Concentrically zoning	Suisari Island (ZF)	Greenish	nodule	micro- and macrocrystalline quartz, length-fast chalcedony	chlorite, epidote, calcite, K-feldspar, titanite, hematite	-	-	

Black agates have been recognised in the upper part of ZF within the Onega Basin. They commonly occur in the inter-pillow lava space as veinlets and nodules. Agates exhibit alternating white and absolutely black opaque zones, significantly varying in number and size. Three main morphological types were distinguished in black agates from ZF, including monocentric concentrically zoning, polycentric spherulitic, and moss agates.

Similar to light-coloured agates of the SF [9], the black agates of the ZF are mainly composed of micro- and macro-crystalline quartz, fibrous chalcedony, and quartzine. The absence of other silica phases (opal, cristobalite, tridymite, and moganite) is typical for agates, which are hosted by either relatively old volcanic rocks or rocks that have been subjected to paleo-heating. Such silica phases are metastable and thus tend to transform into water-poor α-quartz [53]. For instance, Raman spectroscopy investigation of agate and chalcedony from younger igneous host rocks of age 13–1100 Ma showed the presence of moganite in all the examined samples [54,55]. No moganite was identified in agates from host rocks that have been subjected to post-deposition paleo-heating. The quartz structure parameters of studied black agates according to the X-ray diffraction data (well-developed reflections of (212), (203), and (301), high crystallinity index CI (9.5–10.3), and absence of moganite) suggest multi-stage silica minerals' recrystallisation due to a metamorphic (thermal) effect [55].

Optical, SEM-EDS, and Raman spectroscopy analyses revealed that the black colour of the studied agates is associated with the presence of carbonaceous matter disseminated in a silica matrix. Thermal analysis indicates a low average concentration of CM in black agates, with a maximum of 0.69 wt.% in the black zones of concentrically zoning agate. SEM-EDS analysis indicated that the concentration of carbon in the black areas in all studied agate samples is twice as high as in light areas. Despite low carbon content (up to 18 wt.%), the dispersed CM provides the deep black colour to some agate areas.

The microscopic observations show that in the CZ agates, CM is mostly concentrated in zones of fine-grained quartz, length-fast chalcedony, and length-slow quartzine, whereas CM produces only rims on the edges of macrocrystalline quartz (Figure 4A,B,D–F). The accumulation of CM at the boundary of quartz crystals may be the result of a "self-purification" mechanism, which has been previously proposed to explain the accumulation of Fe oxides at the boundary between particular chalcedonic spherules [56]. The CM was rejected from the silica during crystallisation, moved with the crystallisation front, and concentrated CM. CM from SP agates is associated mostly with quartzine, whereas the microcrystalline quartz zones are depleted in CM. Similar selective colourification of quartzine layers in Mongoly agates with Fe oxides and hydroxides were reported by Godovikov et al. [3]. It has been shown that concentrating of Fe-inclusions in agate samples are only observed to quartzine layers, whereas in chalcedony layers, Fe-inclusions are absent. Presence of quartzine in agates may point to a deposition in sulphate-rich solutions or evaporitic conditions [57]. However, up to now, the specific physiochemical conditions of agates' formation leading to the formation of quartzine are still poorly understood. In case of moss agates, where only microcrystalline quartz was identified among the silica phases, CM is associated with the quartz grains of smaller size (Figure 5C).

Compared to light-coloured varieties of agates from the ZF and SF, the black agates of the ZF contain lower amounts of micro-inclusions, e.g., chlorite and iron oxides/hydroxides (Table 2), responsible for an additional colour tinge of agates. The black colour of agates is associated only with the disseminated CM in the silica matrix.

6.2. Origin of CM in Agates

Carbon-bearing agates are rare, and the information on CM composition and origin is scarce in the literature. Apart from calcite, carbon can be presented by organic compounds or carbonaceous matter occurring as fluid or solid inclusions in agates. Various hydrocarbon gases (CH_4, C_2H_4, C_2H_6, C_3H_6, C_3H_8) were recorded in fluid inclusions in agates from the epithermal deposits from the Russian Polar Urals [58], that originated from the oil and gas under-layered sedimentary rocks. Solid hydrocarbon (bitumen) inclusions mostly consisting of asphaltenes have been reported for agates from acidic volcanic rocks (Lower Silesia, Poland) [11]. The stable carbon isotope analysis revealed that the bituminous CM had algal or algal-humic origin. For these rocks, the amorphous carbonaceous matter, probably with low content of hydrocarbons, was also recorded in veinlet and moss agates [59]. The carbonaceous matter with various degrees of structural ordering was recognised in agates from Triassic basalts (Meknés-Tafilalet, Asni and Agouim Regions, Morocco) [6,7] and onyx agates from Mali [10]. The CM from Mali agates was attributed to low-crystalline graphite, which might originate from hydrothermal formation of graphite from methane under elevated temperatures or graphitisation of organic precursors by secondary hydrothermal or metamorphic overprint [10].

Raman spectroscopy analysis shows that CM recorded in all types of black agates from ZF correspond to poorly ordered CM [40,41,50–52], however, the structural ordering is different in various agate types.

The relatively ordered CM was recorded in spherulitic and moss agates, which might be attributed to the medium grade CM according to the classification proposed by Kouketsu et al. [45]. It is characterised by high values of R1 close to 1 (R1 = 0.93–1.13), together with low FWHM-D1 = 67–70 cm^{-1} and low intensive disorder-related bands D3 and D4. The Raman spectroscopic features of CM from CZ agates and inter-pillow matrix, namely the low value of R1 = 0.78 accompanied with high FWHM-D1 = 90 cm^{-1}, and the presence of the intensive disorder-related bands D3 and D4, indicated the relatively low degree of ordering. Raman spectra of CM from CZ agates are constituent to the low-grade CM [45].

The empirical thermometers based on Raman spectroscopic features of CM are widely used to determine the metamorphic temperatures of CM [42,52,60–64]. They are based on the principle that the structural ordering of CM is an irreversible process, so the degree of graphitisation is an indicator of maximum temperature of metamorphic transformation, i.e., the structure and the microstructure of CM are unaffected by retrograde metamorphic events [42,65]. Since CMs from black agates were attributed to low- and medium-grade CM, we applied the Raman spectroscopy thermometer proposed by Kouketsu et al. [45] to determine the metamorphic temperature. This thermometer is based on the linear relation between FWHM-D1 and temperature in the range of T = 150–400 °C. The maximum temperatures of thermal transformation of CM from MS and SP agates are close and were determined to be T = 333 ± 1 °C and T = 328 ± 9 °C, respectively. CM from CZ agates experienced thermal transformations at lower temperatures, T = 264 ± 16 °C. It is noteworthy that temperatures determined for CM from CZ agates show significant scattering, indicating high heterogeneity of CM compared to relatively ordered CM from MS and SP agates (Figure 9). CMs from the inter-pillow matrix have intermediate values of methamorphic temperature, T = 299 ± 9 °C. These temperatures are consistent with prehnite-pumpellyite facies and are in agreement with previous studies [35,36].

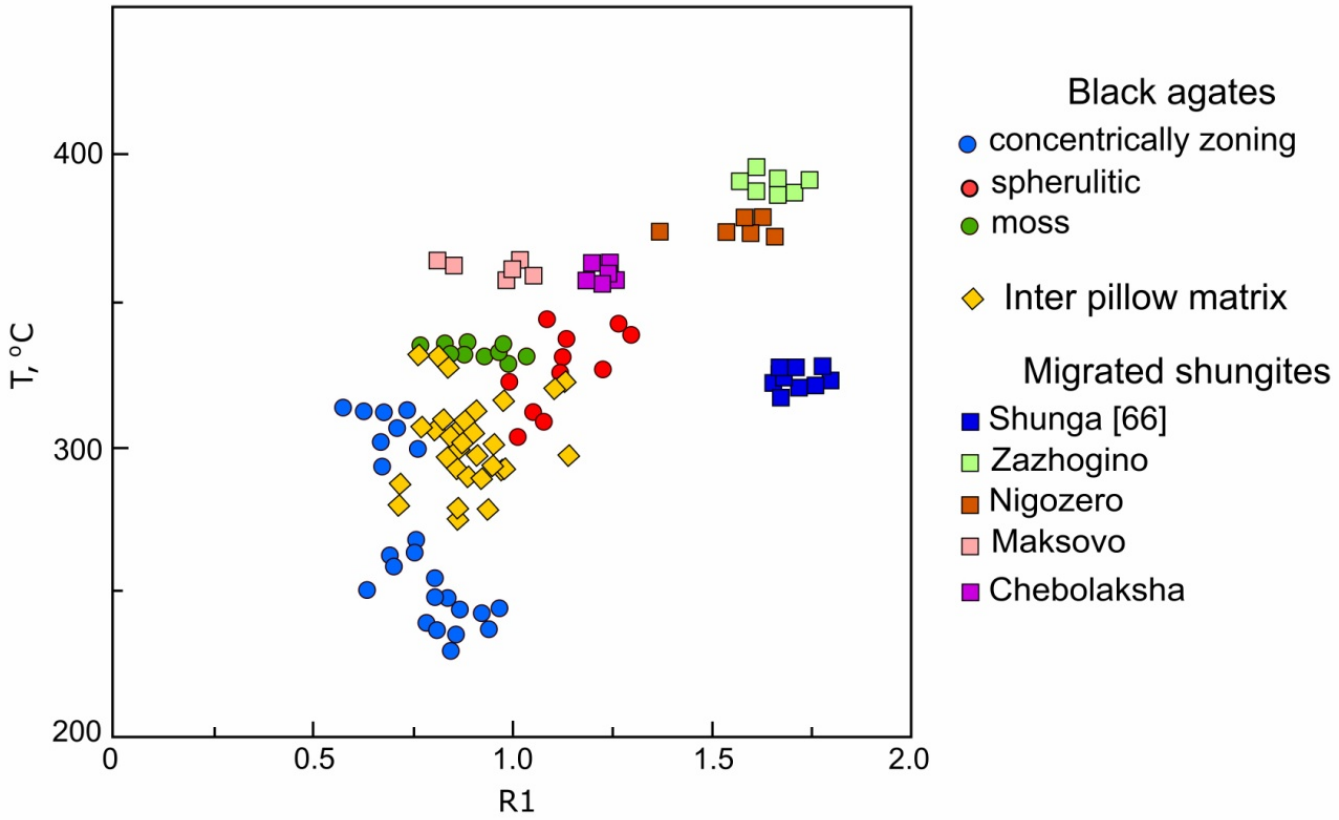

Figure 9. R1 vs. peak metamorphic temperature for the carbonaceous matter from black agates, inter-pillow matrix, and shungites from various deposits. Temperatures were calculated using the thermometer proposed by Kouketsu et al. [45]. Shunga [66].

The following sources of CM in black agates from ZF might be proposed:

1. CM might be incorporated from the inter-pillow matrix considering that initially the inter-pillow matrix might be composed of sedimentary organic matter.
2. CM might be supplied by hydrothermal fluids enriched in CM due to contamination from the host rocks.
3. CM might be formed by the redox reaction between CO_2 and CH_4 in hydrothermal fluids [67,68].

CM from CZ is characterised by high heterogeneity and can be divided into two groups. The first group includes CM with metamorphic temperatures close to 300 °C and similar to that of CM from the inter-pillow matrix (Figure 9), suggesting that CM in CZ agates might be partially incorporated from the inter-pillow matrix. The second group of CM have lower temperatures close to 250 °C and might be produced by the chemical reactions involving CO_2 and/or CH_4 in hydrothermal fluids [69]. Therefore, the data suggest that CM from CZ agates might originate both from the inter-pillow matrix and hydrothermal fluid.

Another possible source of CM in the studied agates might be associated with the underlying carbon-bearing shungite rocks. In order to decipher the model, we compared the metamorphic temperatures determined for migrated shungites from various shungite deposits using the thermometer proposed by Kouketsu et al. [45] with CM from studied agates. Figure 9 shows that CM from MS and SP agates are characterised by the metamorphic temperatures close to migrated shungites (Figure 9). CM from SP agates is characterised by higher heterogeneity than CM from MS agates, and there is a slight overlapping of metamorphic temperatures determined for CM from SP agates and the inter-pillow matrix. Therefore, we cannot exclude that CM from SP agates could partially originate from the CM of the inter-pillow matrix. However, the source of CM in MS and SP

agates is mainly associated with the hydrothermal fluids enriched in mechanically derived CM incorporated from underlying shungite rocks.

6.3. Petrological Implications

Summarizing the data on the geology, geochemistry, and texture of black agates from the upper part of ZF obtained in the present study and the results of a previous study of light-coloured agates from the lower part of SF [9], the agate mineralisation in LSH can be generalised into 2 stages, as illustrated in Figure 10. Agate mineralisation in LSH occurred after the formation of volcanic-sedimentary rocks of ZF (2100–1980 Ma), including carbon-bearing mudstones (Figure 10a) and shungite rocks (ca. 2050 Ma) [31] (Figure 10b)—pre-stage "0".

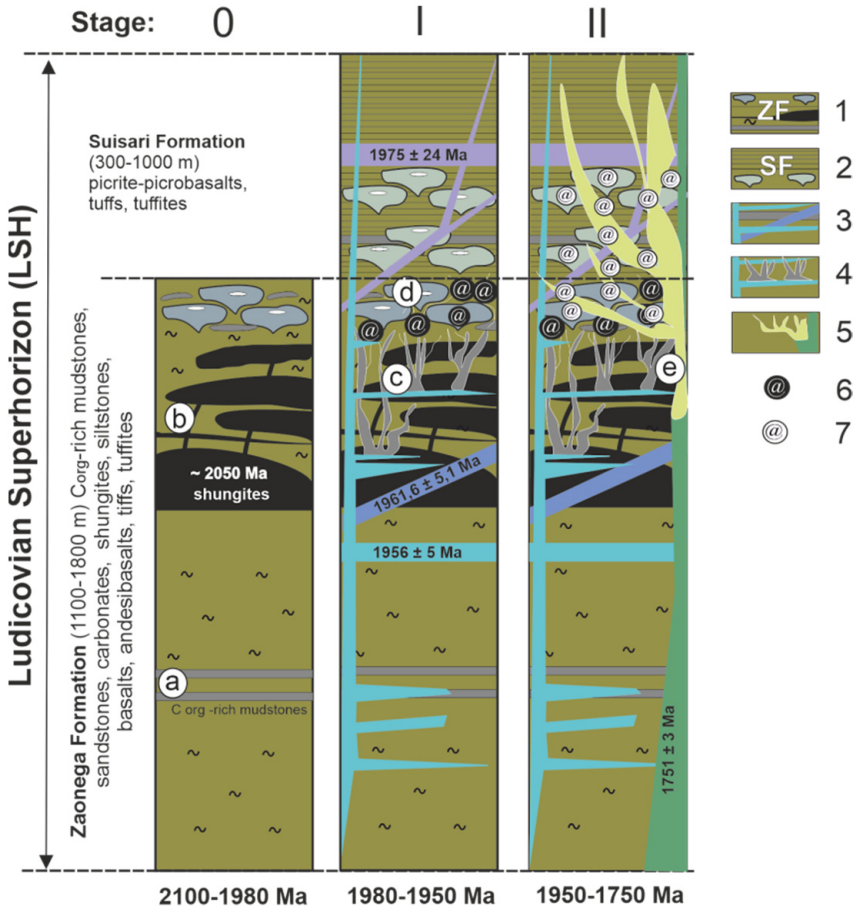

Figure 10. Schematic model of the agate formation stages in the Onega Basin. Compiled using data from [15,18,30,31,70,71]. Legend: Paleoproterozoic, Ludicovian Superhorizon ca. 2100–1920 Ma: 1—C_{org}-rich rocks (shungites), sandstones, siltstones, argillites, carbonates, basalts, andesibasalts, tuffs, tuffites (Zaonega Formation); 2—picrites, picritic basalts, tuffs, tuffites, tuff-conglomerates, gritstones (Suisari Formation); 3—ca. 1975–1956 Ma gabbroids; 4—ca. 1980–1950 Ma hydrothermal fluid flow; 5—ca. 1780–1750 Ma intrusion of gabbro-dolerite sills, hydrothermal fluid flow; 6—black agates; 7—light-coloured agates. Pre-stage 0: formation of carbon-bearing mudstone (**a**) and shungite rocks (**b**) in the volcano-sedimentary succession of the ZF. Stage I: formation of the SF of the volcano-sedimentary succession, multiphase intrusions of peridotite and gabbro-dolerite sills and dikes (**c**), and production of silica-carbonate hydrothermal fluids enriched in CM and formation of black agates in the upper part of ZF (**d**). Stage II: intrusion of gabbro-dolerite sills in the Onega Basin, triggering hydrothermal activity and formation of light-coloured agates in the upper part of ZF and lower part of SF (**e**).

Stage I involves the formation of black agates in the upper part of ZF and is associated with the multiphase intrusions of peridotite and gabbro-dolerite sills and dikes at 1980–1950 Ma [15,30,31] (Figure 10c). This event remobilised the CM from the weakened zones of shungite rocks and produced silica-carbonate hydrothermal fluids enriched in CM. The CM-bearing hydrothermal fluids formed the MS and SP black agates in the upper part of ZF (Figure 10d).

Stage II involves the formation of CZ agates since they contained heterogeneous CM originated both from the inter-pillow matrix and/or hydrothermal fluids. It was associated with a hydrothermal maximum at 1780–1750 Ma, initiated by the intrusion of gabbro-dolerite sills, and occurred at 190 Ma later than the continental flood basalts outflow stage. At this stage, light-coloured agates in both the upper part of ZF and the lower part of SF (Figure 10e) were formed.

7. Conclusions

(1) The present study provided the first detailed investigation of black agates occurring in volcanic rocks of the ZF within the Onega Basin (Karelian Craton, Fennoscandian Shield).
(2) The silica matrix of black agates is only composed by chalcedony, quartz, and quartzine. In addition to silica minerals, calcite, chlorite, feldspar, sulphides, and CM are also identified.
(3) Black colouration of agates is produced by disseminated carbonaceous matter within the silica matrix with a bulk content of less than 1 wt.%.
(4) Three main texture types of black agates were identified: monocentric concentrically zoning, polycentric spherulitic, and moss agates.
(5) The source of CM in moss and spherulitic agates is associated with the hydrothermal fluids enriched in mechanically derived carbonaceous matter incorporated from underlaying shungite rocks. CM from the concentrically zoning agates originate both from the inter-pillow matrix and hydrothermal fluid (i.e., via chemical reactions involving CO_2 and/or CH_4).

The present investigation contributes to understanding possible sources of carbonaceous matter in agates and displays probable mechanisms of redistribution of carbonaceous matter in the hydrothermal systems of the Paleoproterozoic volcanic rocks.

Supplementary Materials: The following are available online at https://www.mdpi.com/article/10.3390/min11090918/s1, Table S1: Chemical composition of black and white agates from the ZF LSH Onega Basin (XRF analysis, wt.%). Table S2: Chemical composition of local (black and white) areas of the agate, EDS microanalysis (wt.%). Table S3: Raman spectral characteristics of CM from black agates and inter-pillow matrix. Figure S1: X-ray diffractograms of the MS and SP agate samples and fragments of X-ray diffractograms in the range of 17–33° 2θ, with the most intense peaks of a-quartz for CZb, CZw, MS, and SP agate samples. Figure S2: Raman spectra of examined agates. (a) Spectrum of black agate area showing characteristic D1 bands at about 1350 cm^{-1} and G bands at about 1600 cm^{-1} of poorly ordered CM, as well as the most intense quartz (Qtz) and calcite (Cal) bands. (b) Spectrum of α-quartz in agate as the only silica phase present. Figure S3: DSC, TG, and DTG curves for examined agate and inter-pillow matrix samples.

Author Contributions: Conceptualisation, E.N.S., S.Y.C. and S.A.S.; investigation, E.N.S., S.Y.C. and S.A.S.; data curation, E.N.S. and S.Y.C.; writing—original draft, E.N.S., S.Y.C. and S.A.S.; writing—review and editing, S.A.S. and A.V.S.; visualisation, E.N.S., S.A.S. and S.Y.C.; supervision, S.A.S. All authors have read and agreed to the published version of the manuscript.

Funding: This research was funded by state assignment to the Institute of Geology Karelian Research Centre RAS.

Data Availability Statement: All data are contained within the article and supplementary materials.

Acknowledgments: We are grateful to S.V. Bordyukh, I.S. Inina, G.S. Ternovaya, and O.V. Bukchina (IG KRC RAS, Petrozavodsk, Russia) for their assistance in analytical investigations. The authors thank O.B. Lavrov (IG KRC RAS, Petrozavodsk, Russia) for consultancy in the field research process. We are grateful to Guest Editor G.A. Palyanova (Novosibirsk, Russia) for the invitation to write this article for the special issue "Agates: types, mineralogy, deposits, host rocks, ages and genesis", the careful analysis of the manuscript, and advice. We would like to deeply acknowledge four anonymous reviewers for their careful revisions and for their interesting suggestions, which helped us to improve the manuscript.

Conflicts of Interest: The authors declare no conflict of interest.

References

1. Moxon, T.; Palyanova, G. Agate Genesis: A Continuing Enigma. *Minerals* **2020**, *10*, 953. [CrossRef]
2. Götze, J.; Möckel, R.; Pan, Y. Mineralogy, geochemistry and genesis of agate—A review. *Minerals* **2020**, *10*, 1037. [CrossRef]
3. Godovikov, A.A.; Ripinen, O.I.; Motorin, S.G. *Agates*; Nedra: Moscow, Russia, 1987; p. 368. (In Russian)
4. Barsanov, G.P.; Yakovleva, V.E. *Mineralogy of Gemstones and Semi-Precious Varieties of Fine-Grained Chalcedony*; Nauka: Moscow, Russia, 1984; 144p. (In Russian)
5. Götze, J.; Tichomirowa, M.; Fuchs, H.; Pilot, J.; Sharp, Z.D. Chemistry of agates: A trace element and stable isotope study. *Chem. Geol.* **2001**, *175*, 523–541. [CrossRef]
6. Natkaniec-Nowak, L.; Dumańska-Słowik, M.; Pršek, J.; Lankosz, M.; Wróbel, P.; Gaweł, A.; Kowalczyk, J.; Kocemba, J. Agates from Kerrouchen (The Atlas Mountains, Morocco): Textural Types and Their Gemmological Characteristics. *Minerals* **2016**, *6*, 77. [CrossRef]
7. Pršek, J.; Dumańska-Słowik, M.; Powolny, T.; Natkaniec-Nowak, L.; Toboła, T.; Zych, D.; Skrepnicka, D. Agates from Western Atlas (Morocco)—Constraints from mineralogical and microtextural characteristics. *Minerals* **2020**, *10*, 198. [CrossRef]
8. Polekhovsky, Y.S.; Punin, Y.O. Agate mineralization in basaltoids of the northeastern Ladoga region, South Karelia. *Geol. Ore Depos.* **2008**, *50*, 642–646. [CrossRef]
9. Svetova, E.; Svetov, S. Mineralogy and Geochemistry of Agates from Paleoproterozoic Volcanic Rocks of the Karelian Craton, Southeast Fennoscandia (Russia). *Minerals* **2020**, *10*, 1106. [CrossRef]
10. Götze, J.; Nasdala, L.; Kempe, U.; Libowitzky, E.; Rericha, A.; Vennemann, T. The origin of black colouration in onyx agate from Mali. *Miner. Mag.* **2012**, *76*, 115–127. [CrossRef]
11. Dumańska-Slowik, M.; Natkaniec-Nowak, L.; Kotarba, M.J.; Sikorska, M.; Rzymełka, J.A.; Łoboda, A.; Gaweł, A. Mineralogical and geochemical characterization of the "bituminous" agates from Nowy Kościol (Lower Silesia). *J. Mineral. Geochem.* **2008**, *184*, 255–268. [CrossRef]
12. Melezhik, V.A.; Medvedev, P.V.; Svetov, S.A. The Onega basin. In *Reading the Archive of Earth's Oxygenation*; Melezhik, V.A., Prave, A.R., Fallick, A.E., Kump, L.R., Strauss, H., Lepland, A., Hanski, E.J., Eds.; Springer: Berlin/Heidelberg, Germany, 2013; pp. 387–490.
13. Svetova, E.N.; Svetov, S.A. Agates from Paleoproterozoic volcanic rocks of the Onega Structure, Central Karelia. *Geol. Ore Depos.* **2020**, *62*, 669–681. [CrossRef]
14. Timofeev, V.M. To the genesis of Zaonega shungite. *Proc. Soc. St. Petersburg Nat.* **1924**, *39*, 99–122. (In Russian)
15. Puchtel, I.S.; Arndt, N.T.; Hofmann, A.W.; Haase, K.M.; Kröner, A.; Kulikov, V.S.; Kulikova, V.V.; Garbe-Schönberg, C.D.; Nemchin, A.A. Petrology of mafic lavas within the Onega plateau, central Karelia: Evidence for 2.0 Ga plume-related continental crustal growth in the Baltic Shield. *Contrib. Mineral. Petrol.* **1998**, *130*, 134–153. [CrossRef]
16. Slabunov, A.I.; Lobach-Zhuchenko, S.B.; Bibikova, E.V.; Sorjonen-Ward, P.; Balagansky, V.V.; Volodichev, O.I.; Shchipansky, A.A.; Svetov, S.A.; Chekulaev, V.P.; Arestova, N.A.; et al. The Archaean nucleus of the Fennoscandian (Baltic) Shield. In *European Lithosphere Dynamics*; Gee, D.G., Stephenson, R.A., Eds.; Memoirs, No. 32; Geological Society: London, UK, 2006; pp. 627–644.
17. Arestova, N.A.; Chekulaev, V.P.; Lobach-Zhuchenko, S.B.; Kucherovskii, G.A. Formation of the Archean crust of the ancient Vodlozero domain (Baltic shield). *Stratigr. Geol. Correl.* **2015**, *23*, 119–130. [CrossRef]
18. Kulikov, V.S.; Svetov, S.A.; Slabunov, A.I.; Kulikova, V.V.; Polin, A.K.; Golubev, A.I.; Gorkovets, V.Y.; Ivashchenko, V.I.; Gogolev, M.A. Geological map of Southeastern Fennoscandia (scale 1:750,000): A new approach to map compilation. *Trans. KarRC RAS* **2017**, *2*, 3–41. [CrossRef]
19. Stepanova, A.V.; Samsonov, A.V.; Salnikova, E.B.; Puchtel, I.S.; Larionova, Y.O.; Larionov, A.N.; Stepanov, V.S.; Shapovalov, Y.B.; Egorova, S.V. Palaeoproterozoic Continental MORB-type Tholeiites in the Karelian Craton: Petrology, Geochronology, and Tectonic Setting. *J. Petrol.* **2014**, *55*, 1719–1751. [CrossRef]
20. Kulikov, V.S.; Kulikova, V.V.; Lavrov, B.S.; Pisarevskii, S.A.; Pukhtel, I.S.; Sokolov, S.Y. *The Paleoroterozoic Suisarian Picrite–Basalt Complex in Karelia: Key Section and Petrology*; KNTs RAN: Petrozavodsk, Russia, 1999; 96p. (In Russian)
21. Kulikov, V.S.; Rychanchik, D.V.; Golubev, A.I.; Filippov, M.M.; Tarkhanov, G.V.; Frik, M.G.; Svetov, S.A.; Kulikova, V.V.; Sokolov, S.Y.; Romashkin, A.E. Stratigraphy and magmatism. Ludicovian. In *Paleoproterozoic Onega Structure: Geology, Tectonics, Structure, and Metallogeny*; Glushanin, L.V., Sharov, N.V., Shchiptsov, V.V., Eds.; Karelian Research Centre, RAS: Petrozavodsk, Russia, 2011; pp. 67–101. (In Russian)

22. Galdobina, L.P. The Ludicovian Superhorizon. In *Geology of Karelia*; Sokolov, V.A., Ed.; Nauka: Leningrad, Russia, 1987; pp. 59–67. (In Russian)
23. Buseck, P.R.; Galdobina, L.P.; Kovalevski, V.V.; Rozkova, N.N.; Valley, J.W.; Zaidenberg, A.Z. Shungites: The C-rich rocks of Karelia, Russia. *Can. Mineral.* **1997**, *35*, 1363–1378.
24. Melezhik, V.A.; Fallick, A.E.; Filippov, M.M.; Larsen, O. Karelian shungite—An indication of 2.0-Ga-old metamorphosed oil-shale and generation of petroleum: Geology, lithology and geochemistry. *Earth Sci. Rev.* **1999**, *47*, 1–40. [CrossRef]
25. Melezhik, V.A.; Fallick, A.E.; Filippov, M.M.; Lepland, A.; Rychanchik, D.V.; Deines, Y.E.; Medvedev, P.V.; Romashkin, A.E.; Strauss, H. Petroleum surface oil seeps from a Paleoproterozoic petrified giant oilfield. *Terra Nova* **2009**, *21*, 119–126. [CrossRef]
26. Kump, L.R.; Junium, C.; Arthur, M.A.; Brasier, A.; Fallick, A.; Melezhik, V.; Lepland, A.; Črne, A.E.; Luo, G.M. Isotopic evidence for massive oxidation of organic matter following the great oxidation event. *Science* **2011**, *334*, 1694–1696. [CrossRef]
27. Kovalevskii, S.V.; Moshnikov, I.A.; Kovalevski, V.V. Heat-treated nano-structured shungite rocks and electrophysical properties associated. *Nanosyst. Phys. Chem. Math.* **2018**, *9*, 468–472. [CrossRef]
28. Filippov, M.M. *Shungite Rocks of the Onega Structure*; KarNTs RAN: Petrozavodsk, Russia, 2002; 282p. (In Russian)
29. Inostrantsev, A.A. New end member of amorphous carbon. *Gorn. J.* **1897**, *2*, 314–342. (In Russian)
30. Stepanova, A.V.; Samsonov, A.V.; Larionov, A.N. The final episode of the middle proterozoic magmatism in the Onega structure: Data on Trans-Onega dolerites. *Trans. KarRC RAS* **2014**, *1*, 3–16.
31. Martin, A.P.; Prave, A.R.; Condon, D.J.; Lepland, A.; Fallick, A.E.; Romashkin, A.E.; Medvedev, P.V.; Rychanchik, D.V. Multiple Palaeoproterozoic carbon burial episodes and excursions. *Earth Planet. Sci. Lett.* **2015**, *424*, 226–236. [CrossRef]
32. Gudin, A.N.; Dubinina, E.O.; Nosova, A.A. Petrogenesis of Variolitic Lavas of the Onega Structure, Central Karelia. *Petrology* **2012**, *20*, 255–270. [CrossRef]
33. Svetov, S.A.; Chazhengina, S.J. Geological Phenomenon of Yalguba RidgeVariolite from F. Yu. Levinson-Lessing's Time until Today: Mineralogical and Geochemical Aspects. *Geol. Ore Depos.* **2018**, *60*, 547–558. [CrossRef]
34. Svetov, S.A.; Chazhengina, S.Y.; Stepanova, A.V. Geochemistry and texture of clinopyroxene phenocrysts from Paleoproterozoic picrobasalts, Onega Basin, Fennoscandian Shield: Records of magma mixing processes. *Minerals* **2020**, *10*, 434. [CrossRef]
35. Leonov, M.G.; Kulikov, V.S.; Zykov, D.S.; Kolodyazhny, S.Y.; Poleshchuk, A.V. Tectonics. In *Paleoproterozoic Onega Structure: Geology, Tectonics, Structure, and Metallogeny*; Glushanin, L.V., Sharov, N.V., Shchiptsov, V.V., Eds.; Karelian Research Centre, RAS: Petrozavodsk, Russia, 2011; pp. 127–170. (In Russian)
36. Spiridonov, E.M.; Putintzeva, E.V.; Lavrov, O.B.; Ladygin, V.M. Kronstedtite, pumpelliite, prehnite and lennilenapeite in the metaagates and metabasalts of the early Proterozoic trap formation in the northern Onega region. In Proceedings of the Conference Lomonosov Readings, Moscow, Russia, 17–27 April 2017; Moscow State University: Moscow, Russia, 2017. Available online: https://conf.msu.ru/file/event/4305/eid4305_attach_b0acc3e7de2cd859225469534617a6272d70ce50.pdf (accessed on 9 July 2021). (In Russian).
37. Filipov, M.M.; Deynes, Y.E. *Subtabular Type of Shungite Deposits of Karelia*; KarSC RAS: Petrozavodsk, Russia, 2018; 261p. (In Russian)
38. Glebovitskii, V.A.; Bushmin, S.A.; Belyatsky, B.V.; Bogomolov, E.S.; Borozdin, A.P.; Savva, E.V.; Lebedeva, Y.M. RB-SR age of metasomatism and ore formation in the low-temperature shear zones of the Fenno-Karelian Craton, Baltic Shield. *Petrology* **2014**, *22*, 184–204. [CrossRef]
39. Bibikova, E.V.; Kirnozova, T.I.; Lazarev, Y.I.; Makarov, V.A.; Nikolaev, A.A. U–Pb isotopic age of the Karelian Vepsian. *Trans. USSR Acad. Sci.* **1990**, *310*, 189–191.
40. Ferrari, A.C.; Robertson, J. Interpretation of Raman spectra of disordered and amorphous carbon. *Phys. Rev.* **2000**, *61*, 14095–14107. [CrossRef]
41. Wopenka, B.; Pasteris, J.D. Structural characterization of kerogens to granulite-facies graphite: Applicability of Raman microprobe spectroscopy. *Am. Mineral.* **1993**, *78*, 533–557.
42. Beyssac, O.; Goffé, B.; Chopin, C.; Rouzaud, J.N. Raman spectra of carbonaceous material in metasediments: A new geothermometer. *J. Metamorph. Geol.* **2002**, *20*, 859–871. [CrossRef]
43. Dippel, B.; Jander, H.; Heintzenberg, J. NIR FT Raman spectroscopic study of flame soot. *J. Aerosol Sci.* **1999**, *30*, 4707–4712. [CrossRef]
44. Lahfid, A.; Beyssac, O.; Deville, E.; Negro, F.; Chopin, C.; Goffé, B. Evolution of the Raman spectrum of carbonaceous material in low-grade metasediments of the Glarus Alps (Switzerland). *Terra Nova* **2010**, *22*, 354–360. [CrossRef]
45. Kouketsu, Y.; Mizukami, T.; Mori, H.; Endo, S.; Aoya, M.; Hara, H.; Nakamura, D.; Wallis, S. A new approach to develop the Raman carbonaceous material geothermometer for low-grade metamorphism using peak width. *Isl. Arc.* **2014**, *23*, 33–50. [CrossRef]
46. Murata, J.; Norman, M.B. An index of crystallinity for quartz. *Am. J. Sci.* **1976**, *276*, 1120–1130. [CrossRef]
47. Kuznetsov, S.K.; Svetova, E.N.; Shanina, S.N.; Filippov, V.N. Minor Elements in Quartz from Hydrothermal-Metamorphic Veins in the Nether Polar Ural Province. *Geochemistry* **2012**, *50*, 911–925. [CrossRef]
48. Behera, D.; Nandi, B.K.; Bhattacharya, S. Chemical properties and combustion behavior of constituent relative density fraction of a thermal coal. *Energy Sources Part A Recovery Util. Environ. Eff.* **2019**, *41*, 654–664. [CrossRef]

49. Wada, H.; Tomita, T.; Matsuura, K.; Iuchi, K.; Ito, M.; Morikiyo, T. Graphitization of carbonaceous matter during metamorphism with references to carbonate and pelitic rocks of contact and regional metamorphisms, Japan. *Contrib. Mineral. Petrol.* **1994**, *118*, 217–228. [CrossRef]
50. Kholodkevich, S.V.; Berezkin, V.I.; Davydov, V.Y. Specific structural features and thermal resistance of shungite carbon to graphitization. *Phys. Solid State* **1999**, *41*, 1291–1294. [CrossRef]
51. Jehlicka, J.; Urban, O.; Pokorný, J. Raman spectroscopy of carbon and solid bitumens in sedimentary and metamorphic rocks. *Spectrochim. Acta* **2003**, *59*, 2341–2352. [CrossRef]
52. van Zuilen, M.A.; Fliegel, D.; Wirth, R.; Lepland, A.; Qu, Y.; Schreiber, A.; Romashkin, A.E.; Philippot, P. Mineral-templated growth of natural graphite films. *Geochim. Cosmochim. Acta* **2012**, *83*, 252–262. [CrossRef]
53. Moxon, T.; Carpenter, M.A. Crystallite growth kinetics in nanocrystalline quartz (agate and chalcedony). *Miner. Mag.* **2009**, *73*, 551–568. [CrossRef]
54. Moxon, T.; Nelson, D.R.; Zhang, M. Agate recrystallization: Evidence from samples found in Archaean and Proterozoic host rocks, Western Australia. *Austr. J. Earth Sci.* **2006**, *53*, 235–248. [CrossRef]
55. Moxon, T.; Reed, S.J.; Zhang, M. Metamorphic effects on agate found near the Shap granite, Cumbria, England: As demonstrated by petrography, X-ray diffraction and spectroscopic methods. *Miner. Mag.* **2007**, *71*, 461–476. [CrossRef]
56. Götze, J.; Möckel, R.; Kempe, U.; Kapitonov, I.; Vennemann, T. Origin and characteristics of agates in 1479 sedimentary rocks from the Dryhead area, Montana/USA. *Min. Mag.* **2009**, *73*, 673–690.
57. Folk, R.L.; Pittman, J.S. Length-slow chalcedony; A new testament for vanished evaporates. *J. Sediment. Petrol.* **1971**, *41*, 1045–1058.
58. Silaev, V.I.; Shanina, S.N.; Ivanovskii, V.S. Inclusions of oil gases in agate-type secretions: Implications for forecast of the oil- and gas-bearing potential of the Polar Urals. *Dokl. Earth Sci.* **2002**, *383*, 246–252. (In Russian)
59. Powolny, T.; Dumańska-Słowik, M.; Sikorska-Jaworowska, M.; Wójcik-Baniaaet, M. Agate mineralization in spilitized Permian volcanics from "Borówno" quarry (Lower Silesia, Poland)—Microtextural, mineralogical, and geochemical constraints. *J. Ore Geol. Rev.* **2019**, *114*, 103–130. [CrossRef]
60. Sforna, C.; van Zuilen, M.A.; Philippot, P. Structural characterization by Raman hyperspectral mapping of organic carbon in the 3.46 billion-year-old Apex chert, Western Australia. *Geochim. Cosmochim. Acta* **2014**, *124*, 18–33. [CrossRef]
61. Rantitsch, G.; Grogger, W.; Teichert, C.; Ebner, F.; Hofer, C.; Maurer, E.M.; Schaffer, B.; Toth, M. Conversion of carbonaceous material to graphite within the Greywacke Zone of the Eastern Alps. *Int. J. Earth Sci. Geol. Rundsch.* **2004**, *93*, 959. [CrossRef]
62. Rahl, J.M.; Anderson, K.M.; Brandon, M.T.; Fassoulas, C. Raman spectroscopic carbonaceous material thermometry of low-grade metamorphic rocks: Calibration and application to tectonic exhumation in Crete, Greece. *Earth Planet. Sci. Lett.* **2005**, *240*, 339–354. [CrossRef]
63. Aoya, M.; Kouketsu, Y.; Endo, S.; Shimizu, H.; Mizukami, T.; Nakamura, D.; Wallis, S. Extending the applicability of the Raman carbonaceous-material geothermometer using data from contact metamorphic rocks. *J. Metamorph. Geol.* **2010**, *28*, 895–914. [CrossRef]
64. Wiederkehr, M.; Bousquet, R.; Ziemann, M.; Berger, A.; Schmid, S. 3–D assessment of peak–metamorphic conditions by Raman spectroscopy of carbonaceous material: An example from the margin of the Lepontine dome (Swiss Central Alps). *Int. J. Earth Sci.* **2011**, *100*, 1029. [CrossRef]
65. Buseck, P.R.; Beyssac, O. From Organic Matter to Graphite: Graphitization. *Elements* **2014**, *10*, 421–426. [CrossRef]
66. Chazhengina, S.Y.; Kovakevski, V.V. Raman spectroscopy of weathered shungites. *J. Raman Spectrosc.* **2017**, *48*, 1590–1596. [CrossRef]
67. Manning, C.E.; Shock, E.L.; Sverjensky, D.A. The chemistry of carbon in aqueous fluids at crustal and upper-mantle conditions: Experimental and theoretical constraints. *Rev. Mineral. Geochem.* **2013**, *75*, 109–148. [CrossRef]
68. Kríbek, B.; Sykorová, I.; Machovic, V.; Knésl, I.; Laufek, F.; Zachariás, J. The origin and hydrothermal mobilization of carbonaceous matter associated with Paleoproterozoic orogenic-type gold deposits of West Africa. *Precambrian Res.* **2015**, *270*, 300–317. [CrossRef]
69. Foustoukos, D.I. Metastable equilibrium in the C H O system: Graphite deposition in crustal fluids. *Am. Mineral.* **2012**, *97*, 1373–1380. [CrossRef]
70. Hannah, J.L.; Stein, H.J.; Yang, G.; Zimmerman, A.; Melezhik, V.A.; Filippov, M.M.; Turgeon, S.C. Re—Os geochronology of a 2.05 Ga fossil oil field near Shunga, Karelia, NW Russia. In Proceedings of the Abstracts of the 33 International Geological Congress, Oslo, Norway, 5–14 August 2008.
71. Lubnina, N.V.; Pisarevsky, S.A.; Söderlund, U.; Nilsson, M.; Sokolov, S.J.; Khramov, A.N.; Iosifidi, A.G.; Ernst, R.; Romanovskaya, M.A.; Pisakin, B.N. New palaeomagnetic and geochronological data from the Ropruchey sill (Karelia, Russia): Implications for late Paleoproterozoic palaeogeography. In Proceedings of the Supercontinent Symposium 2012−Programm and Abstracts, Espoo, Finland, 25–28 September 2012; University of Helsinki: Espoo, Finland, 2012; pp. 81–82. Available online: https://tupa.gtk.fi/julkaisu/erikoisjulkaisu/ej_084.pdf (accessed on 9 August 2021).